Solid-State Reaction Synthesis of CoSb2O6-Based Electrodes Towards Oxygen Evolution Reaction in Acidic Electrolytes: Effects of Calcination Time and Temperature

(Article begins on next page)

19 February 2025

Article

Solid-State Reaction Synthesis of CoSb$_2$O$_6$-Based Electrodes Towards Oxygen Evolution Reaction in Acidic Electrolytes: Effects of Calcination Time and Temperature

Francesco Vanzetti, Hilmar Guzmán and Simelys Hernández *

CREST Group, Department of Applied Science and Technology (DISAT), Politecnico di Torino, C.so Duca degli Abruzzi, 24, 10129 Turin, Italy; francesco.vanzetti@polito.it (F.V.); hilmar.guzman@polito.it (H.G.)
* Correspondence: simelys.hernandez@polito.it

Abstract: Mitigating global warming necessitates transitioning from fossil fuels to alternative energy carriers like hydrogen. Efficient hydrogen production via electrocatalysis requires high-performance, stable anode materials for the oxygen evolution reaction (OER) to support the hydrogen evolution reaction (HER) at the cathode. Developing noble metal-free electrocatalysts is therefore crucial, particularly for acidic electrolytes, to avoid reliance on scarce and expensive metals such as Ir and Ru. This study investigates a low-cost, solvent-free solid-state synthesis of CoSb$_2$O$_6$, focusing on the influence of calcination time and temperature. Six samples were prepared and characterized using powder X-ray diffraction (PXRD), energy-dispersive X-ray spectroscopy (EDX), Brunauer–Emmett–Teller (BET) analysis, field-emission scanning electron microscopy (FESEM), and electrochemical techniques. A non-pure CoSb$_2$O$_6$ phase was observed across all samples. Electrochemical testing revealed good short-term stability; however, all samples exhibited Tafel slopes exceeding 200 mV dec^{-1} and overpotentials greater than 1 V. The sample calcined at 600 °C for 6 h showed the best performance, with the lowest Tafel slope and overpotential, attributed to its high CoSb$_2$O$_6$ content and maximized {110} facet exposure. This work highlights the role of calcination protocols in developing Co-based OER catalysts and offers insights for enhancing their electrocatalytic properties.

Keywords: cobalt antimonate; oxygen evolution reaction; acidic electrolyte; hydrogen production

1. Introduction

Global warming represents one of the most significant challenges currently confronting humanity, driving efforts to harness various sustainable energy sources to meet rising global demand [1,2]. Among these, water splitting has emerged as a promising technology, offering an environmentally friendly method for generating high-purity green hydrogen [3]. The production of green hydrogen is critical due to its extensive applications, including its role as a feedstock in methanol synthesis, ammonia production via the Haber–Bosch process, and crude oil hydrocracking, as well as its use as an energy carrier for fueling vehicles. The anodic OER can proceed in either alkaline or acidic media. However, the limited stability of most transition metal oxides under acidic conditions has led to a focus on developing noble metal-free electrocatalysts optimized for alkaline OER [4]. Nonetheless, acidic media are employed in proton exchange membrane (PEM) electrolyzers, which are regarded as one of the most promising technologies for producing high-purity green hydrogen. In recent years, various classes of materials have been explored for OER to reduce noble metal content, including perovskite oxides, pyrochlore oxides, single-atom

catalysts, and ligand-stabilized noble metals [5–10]. Additionally, research has focused on noble metal-free materials, such as first-row transition metal oxides, transition metal chalcogenides, borides, and antimonates [11–13]. In order to develop stable electrocatalysts for OER in acid, it is necessary to identify those phases that are stable under the operative conditions. The Pourbaix diagram of Sb_2O_5 shows the stability in the acid pH window. Sb_2O_5 has low conductivity and is known to not be active towards any electrochemical oxidation processes [14]. The synthesis of materials with two metallic atoms can lead to a cooperative synergistic effect which combines the stability of the first metal atom with the activity of the second, such as Mn/Co and Sb. MnO_2 presents a region of the Pourbaix diagram at pH = 0 where stability is predicted. Previous studies demonstrated this stability for 8 h in a solution 0.5 M H_2SO_4 at a current density of 0.1 mA cm^{-2}, which is 100 times lower than the water splitting device targets [15]. The main issue presented by Mn is associated with dissolution in acidic electrolytes over time. For this reason, Co was employed to reduce the dissolution rate. Mondschein et al. have reported the stability of Co_3O_4 in 0.5M H_2SO_4 solution at 10 mA cm^{-2} for over 12 h with a moderate overpotential of 570 mV [16]. Within the class of antimonates, cobalt antimonate ($CoSb_2O_6$) has shown promise across applications including dye degradation, gas sensing, photocatalysis, solar cell electrodes, and electrocatalysis [17–21].

This critical study investigates the effects of calcination time and temperature on the solid-state synthesis of cobalt antimonate ($CoSb_2O_6$), a method chosen for its advantages of high yield, lower environmental impact, and greater industrial feasibility [22]. Alternative synthetic methods have also been reported, such as electrodeposition [17], the Pechini method [23], colloidal synthesis [24], and gel-combustion synthesis [25]. However, to our knowledge, no prior studies have investigated the solid-state reaction (SSR) synthetic approach for $CoSb_2O_6$ in electrochemical applications. The SSR has the principal advantage of not using solvents, which is the first cause of pollution in wet chemical synthesis. Avoiding their use is one of Green Chemistry's milestones. Other significant advantages of the SSR method include the simplicity of the process and material handling, the low cost of raw materials, cheap equipment, and high yield. Additionally, this study demonstrates the favorable short-term OER stability of $CoSb_2O_6$-based electrodes in acidic media.

## 2. Results and Discussion

2.1. PXRD

Initial powder X-ray diffraction (PXRD) measurements were conducted on the samples, with PXRD patterns for samples calcined for 6 h and 12 h shown in Figure 1a,b, respectively. PXRD data were further analyzed by calculating the ratio between the peaks at 27° and 35°, corresponding to the (110) and (103) facets of $CoSb_2O_6$ [24,26,27], and its crystallites size (see Figure 2). These analyses aimed to identify any preferential growth of crystalline facets and to correlate catalyst activity with morphological characteristics. Notably, distinct outcomes were observed for the 6-h samples. For facet (110) (see Figure 3a and Table S1), the crystallite size decreases as the temperature decreases, while for facet (103) (see Figure 3b and Table S1), the crystallite size shows the opposite trend, increasing as the temperature decreases. Figure 2b presents the data for samples calcined for 12 h, where the trends of facets (110) and (103) contrast with those seen in the 6 h samples. Specifically, in the 12-h samples, the crystallite size of the facet (110) (see Figure 3a and Table S2) decreases with increasing temperature, whereas the crystallite size of facet (103) increases with decreasing temperature. This same trend is observed in the peak ratio for the 6-h samples as well (see Figure 2a).
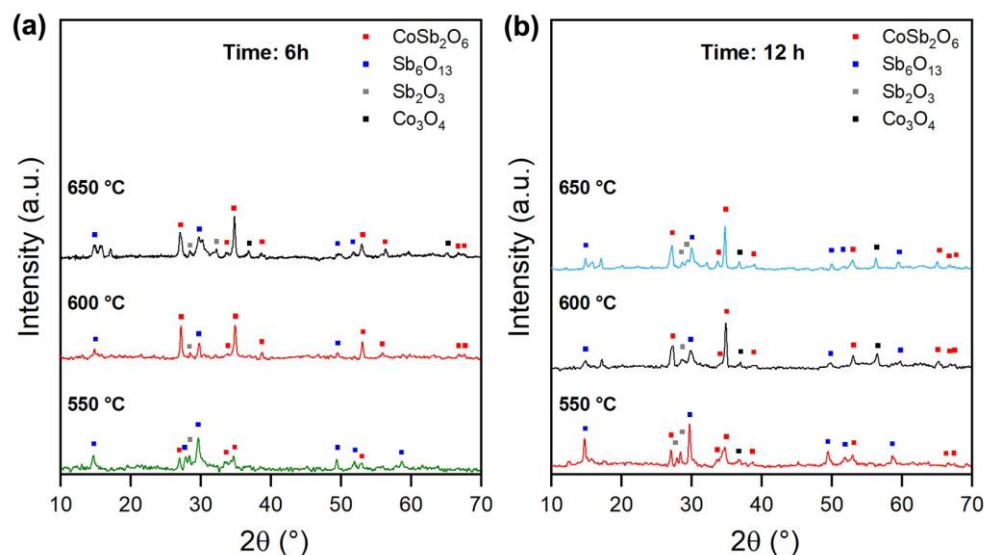
**Figure 1.** PXRD pattern of CoSb$_2$O$_6$ catalysts calcined 550 °C, 600 °C, and 650 °C for (**a**) 6 h; (**b**) 12 h.
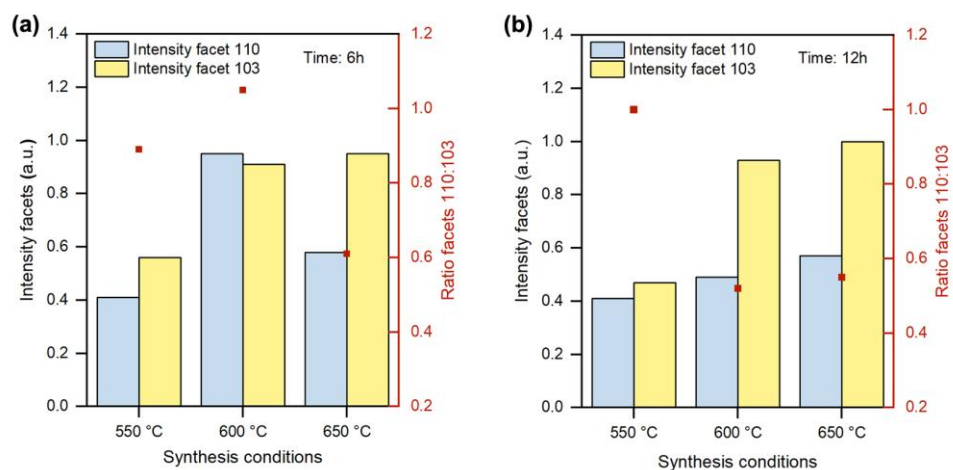
Figure 2. PXRD data, peak intensities related to CoSb$_2$O$_6$ facets 110 and 103 and ratio 110:103 for samples calcined for (**a**) 6 h; (**b**) 12 h. The red dots indicate the ratio facets 110:103.
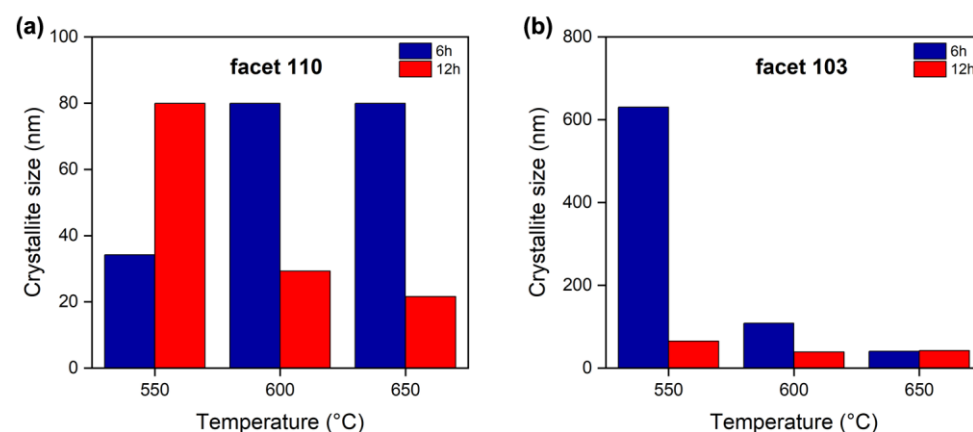
Figure 3. PXRD data, crystallite size comparison between (**a**) facets 110 and (**b**) facets 103 of 6 and 12 h samples. Source data are reported in Table S1 and S2.

The phase diagram reported at 873 K in Figure 4 demonstrates the stability of three primary phases identified in each sample: CoSb$_2$O$_6$, Co$_3$O$_4$ and, Sb$_2$O$_3$, all of which are inherently stable. A fourth phase, Sb$_6$O$_{13}$, is not represented in the diagram, as it requires

an additional energy of 0.025 eV/atom. Despite this requirement, Sb_6O_{13} can be reasonably considered comparably stable to the other phases.
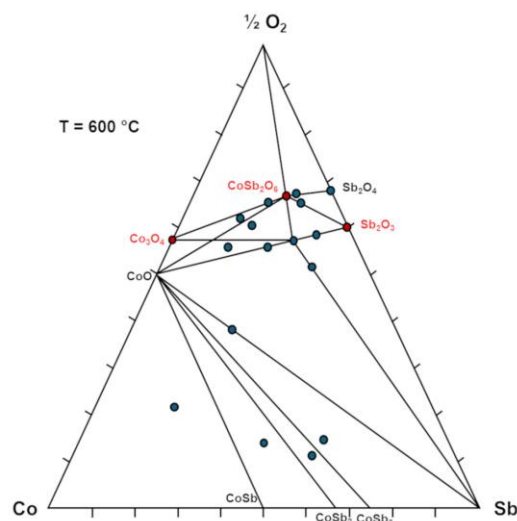
Figure 4. Phase diagram of Co-Sb-O materials synthetized at 600 °C in air. In red are highlighted the phases of interest. Adapted from [25].

Furthermore, since the calcination step was conducted under static air conditions, it was not possible to control the oxygen content during this stage of the process. The (Co+Sb)/O ratio, calculated against the theoretical value of 0.50, confirmed the highest yield of $CoSb_2O_6$ calcined at 600 °C for 6 h, which respects this ratio. The closer the (Co+Sb)/O ratio is to 0.50, the higher the content of $CoSb_2O_6$, as displayed in Figure 5. The stability of the multiple phases in the samples and the oxygen content could be considered responsible for the obtained catalysts.
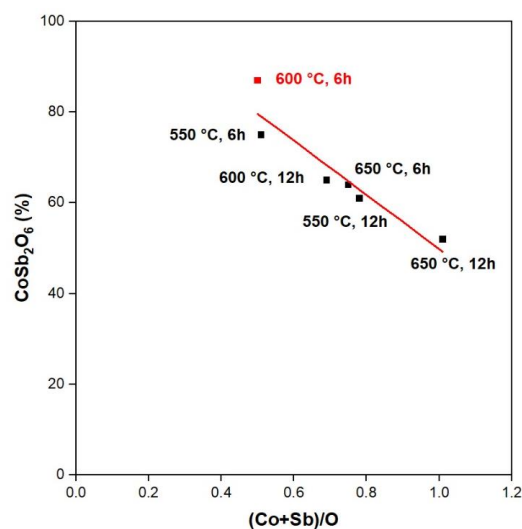

Figure 5. Dependence of $CoSb_2O_6$ content against (Co+Sb)/O ratio. Source data are reported in Table S3.

2.2. EDX

PXRD data combined to semiquantitative Energy Dispersive X-ray (EDX) analyses allowed for a comparative assessment of each sample's composition, including the phase percentages (see Figure 6) and atomic percentages of the catalyst components (see Figure 7). In several samples, the expected theoretical ratios for Sb/Co and O/Sb, set at 2:1 and 3:1, respectively, for $CoSb_2O_6$ formation, were not fully attained. $CoSb_2O_6$ was identified in the X-ray diffraction patterns of all samples (see Figure 6), with the highest concentration

observed in the sample calcined at 600 °C for 6 h. Notably, when comparing samples synthesized for 6 and 12 h, the $CoSb_2O_6$ content consistently increases at 600 °C. However, a decrease in the $CoSb_2O_6$ concentration is observed at higher temperatures, likely due to the preferential formation of refractory phases such as Co_3O_4, which forms between 600 and 700 °C. According to phase quantification, using the HighScore Plus software (version 3.0.5) PXRD tool [28], this sample exhibits the lowest content of other Sb and Co oxides. These findings underscore the challenge of obtaining a pure $CoSb_2O_6$ phase without other oxide phases, consistent with previous studies [18,23,25]. Generally, extended calcination times and elevated temperatures do not enhance $CoSb_2O_6$ formation. Additionally, Sb_6O_{13} content remains constant across all conditions, showing no significant dependence on time or temperature.
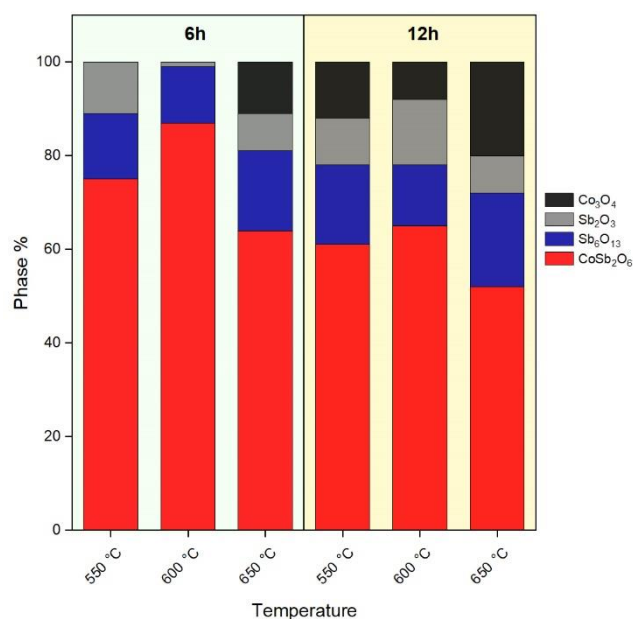
Figure 6. Composition of the crystalline phases of $CoSb_2O_6$ samples synthetized at different calcination time and temperatures as calculated from the PXRD data. The wt. % of each sample is reported. Source data are reported in Table S4.
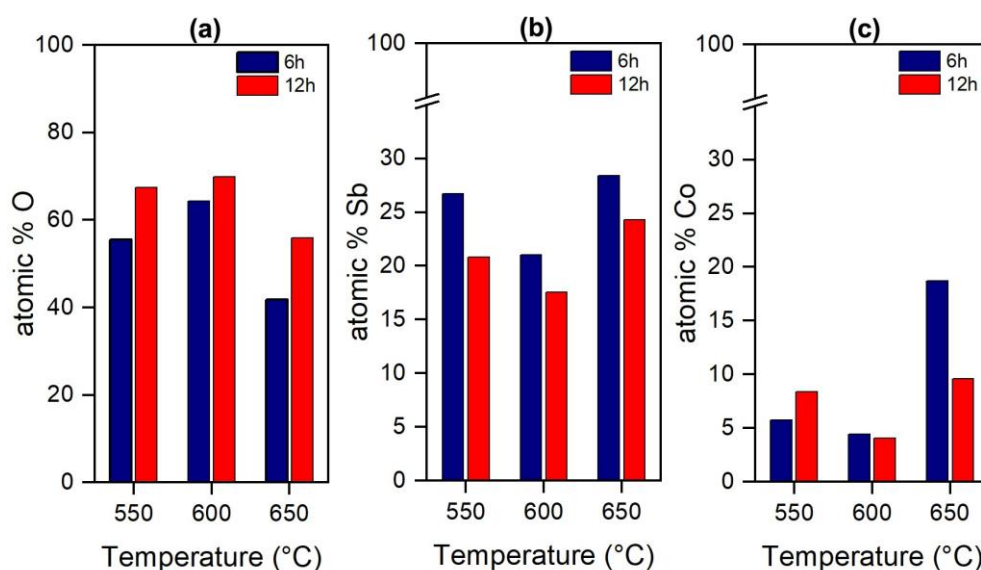
Figure 7. EDX analyses, (**a**) atomic % O; (**b**) atomic % Sb; (**c**) atomic % Co for 6 and 12 h samples. Source data are reported in Table S5.

As shown in Figure 7, samples synthesized over 6 and 12 h exhibit distinct trends in atomic percentage composition. Specifically, oxygen content decreases at higher temperatures, while for samples calcined at 600 °C, both Co and Sb contents are observed to be at their lowest levels.

2.3. BET

BET (Brunauer–Emmet–Teller) measurements were carried out to determine the porosity of the samples. Figures S1 and S3 and Table S6 show the data related to the $CoSb_2O_6$ samples calcined for 6 h. These values are at least two times higher than the ones reported in the literature [29]. In general, the $CoSb_2O_6$ samples have a low value of specific surface area (SSA), total pore volume, and average pore width. Based on the average pore size, all the prepared samples can be classified as mesoporous materials because their pore size is between 2 and 50 nm.

A similar trend was obtained with the materials calcined for 12 h (see Figures S2 and S3, and Table S6), but in these cases, the SSA was at least three times higher than the one reported by Gunasooriya et al. [29]. Also, these materials' average pore width is between 2 and 50 nm, being also classified as mesoporous materials. Although the SSAs increased two-fold and three-fold compared to the literature, in both cases, the total pore volume and the average pore width follow the same trend, suggesting a comparable distribution. However, it must be noted that the differences in terms of BET surface areas are within 2 m^2/g, which is within the instrument's precision limit.

2.4. FESEM

The FESEM (Field Emission Scanning Electron Microscopy) images reported in Figures S4 and S5 support the data collected by PXRD and BET analyses of the $CoSb_2O_6$ catalysts. All the samples have low SSA values (see Figure S3) and are considered mesoporous materials. Moreover, as proven by the PXRD patterns, different phases are present in each sample, and this feature is well represented by the different morphologies evidenced in the FESEM images that can be attributed to the heterogeneous composition of the different samples. In general, the FESEM images of the synthesized $CoSb_2O_6$ catalysts were very difficult to collect because of the surface charging effect due to the poor conductivity of the samples, which caused the brightest horizontal lines observed in the images. This feature could be attributed to the presence of Sb oxides rather than $CoSb_2O_6$.

2.5. Electrochemical Performance

The protocol used to test the catalytic activity of the samples is reported in Section 3.5. Comparing the performances of the materials synthesized for 6 h, see Figure 8, the highest current density was achieved with the catalyst calcined at 600 °C. Both other materials, calcined at 550 °C and 650 °C, showed similar current densities of around 15 mA cm^{-2}. Considering the applied potentials, experimentally obtained from the CP analysis and reported versus the standard hydrogen electrode (SHE), the lowest potential value was shown by the $CoSb_2O_6$ at 550 °C for 6 h. Nevertheless, it should be noted that the potential values between the three samples are very close to each other. Noteworthy, the material with the most stable potential is the $CoSb_2O_6$ at 600 °C for 6 h (see Figure 9a). Regarding overpotentials and Tafel slopes (see Figure 10 and Table S7), among the 6 h samples, the lowest values come from the $CoSb_2O_6$ at 600 °C, with an overpotential of 1098 mV and a Tafel slope of 209 mV dec^{-1}. Among the samples synthesized for 12 h, the activity trend shows an increase in the current density in the following order: $CoSb_2O_6$ at 600 °C, $CoSb_2O_6$ at 550 °C, and $CoSb_2O_6$ at 650 °C. Also for the 12 h samples, there are tiny differences between the potential values recorded with the CP (less than 100 mV, see Figure 9b).
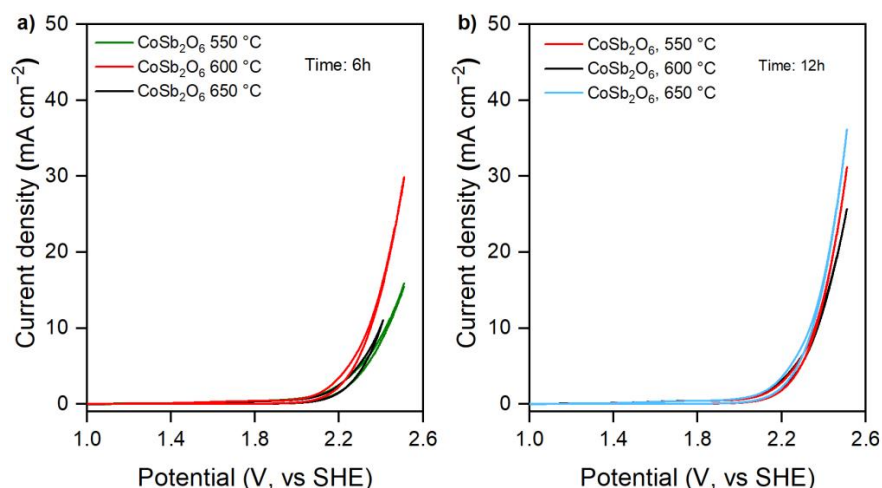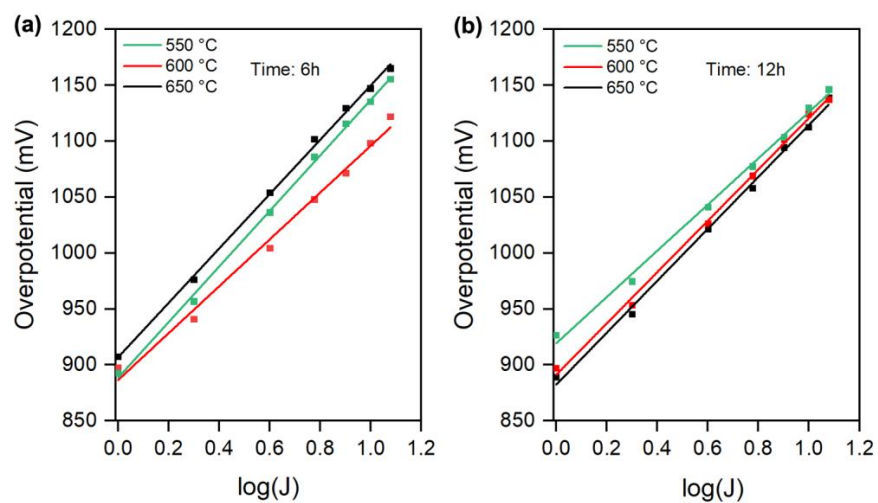
Figure 8. RDE analyses; CV comparison of all different samples of $CoSb_2O_6$ synthetized under different temperature conditions for (**a**) 6 h and (**b**) 12 h.
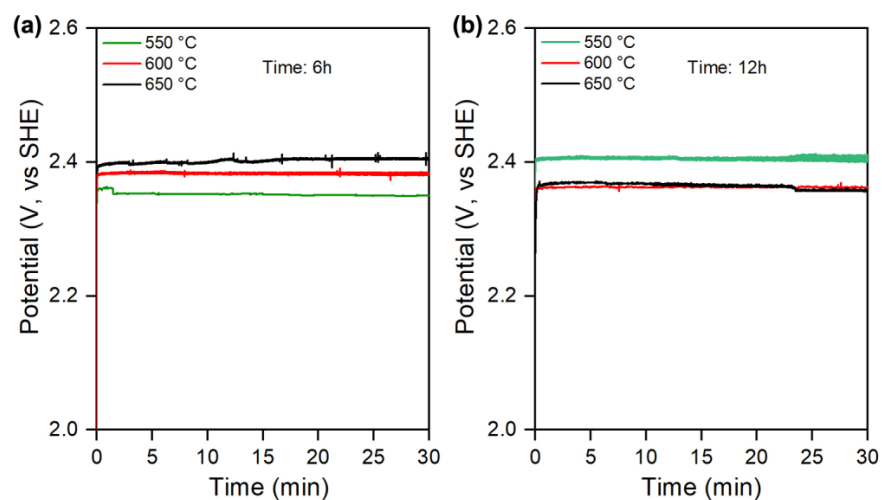
Figure 9. RDE analyses; CP comparison of all different samples of $CoSb_2O_6$ synthetized under different temperature conditions for (**a**) 6 h and (**b**) 12 h.


Figure 10. RDE analyses; Tafel plot comparison of all different samples of $CoSb_2O_6$ synthetized under different temperature conditions for (**a**) 6 h and (**b**) 12 h.

All the $CoSb_2O_6$ samples exhibit good stability throughout the electrochemical tests. The electrocatalyst synthesized at 600 °C for 6 h demonstrates the best performance among

the series, as shown by its relatively lower overpotential and Tafel slope (see Figure 11). This behavior can be attributed to the higher proportion of $CoSb_2O_6$ in this sample, as supported by the EDX analysis.
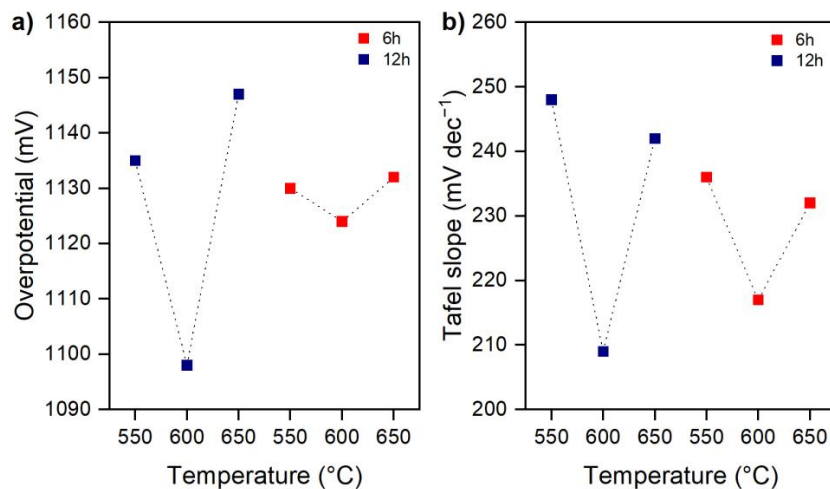
Figure 11. Comparison between calcination conditions with (**a**) Tafel slopes and (**b**) overpotentials.

A comparison with state-of-the-art electrocatalysts is provided in Table S8. While the overpotential of our $CoSb_2O_6$ material is higher than many state-of-the-art electrocatalysts, its performance provides valuable insight into the potential of $CoSb_2O_6$ as an electrocatalyst. Unlike many of the materials in the table, our catalyst is synthesized through a simple, scalable process and does not rely on costly elements or complex architectures. This positions $CoSb_2O_6$ as a promising material for future optimization, especially in applications prioritizing cost efficiency and synthesis scalability over peak performance.

In Figure 12a, the ratio of facets 110:103 of the $CoSb_2O_6$ phase is reported as a function of overpotential, while in Figure 12b, the relation between SSA and the overpotential is shown. It is interesting to note that the overpotential is minimized in correspondence to the ratio of 110:103 facets equal to 1.0, which indicates a higher activity of the (101) facet of $CoSb_2O_6$. Furthermore, the overpotential decreases when the SSA increases, probably due the increment of the number of active sites exposed. However, the most important parameter is the high content of $CoSb_2O_6$, which determines the break of the linear relationship between overpotential and SSA, as displayed by the red dot in Figure 12b, representing the sample at 600 °C for 6 h that contains the higher amount of such a phase.
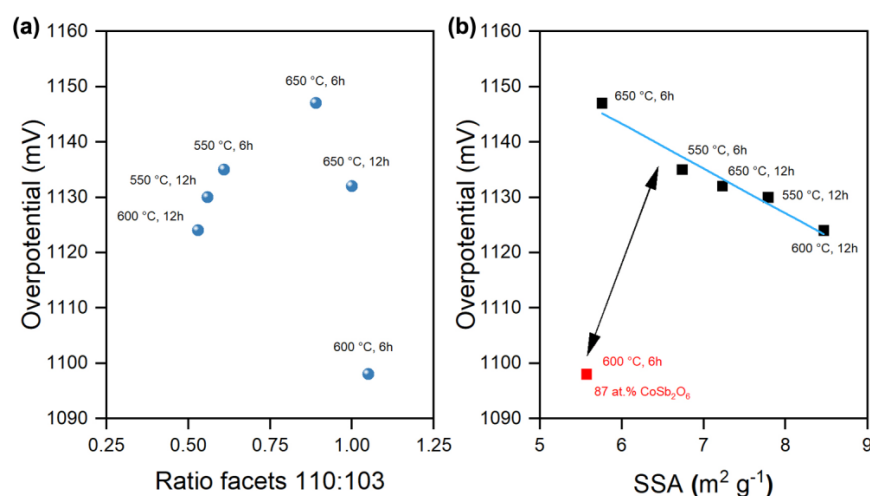
Figure 12. (**a**) Influence of ratio facets 110:103 towards overpotential and (**b**) SSA in relation to overpotential. The best prepared catalyst is highlighted in red.

3. Materials and Methods

3.1. Materials

The reagents and solvents employed, i.e., $CoCl_2 \cdot 6H_2O$ ($\geq$97%, Sigma Aldrich, Milan, Italy), $C_8H_4K_2O_{12}Sb_2 \cdot H_2O$ ($\geq$99%, Sigma Aldrich, Milan, Italy), and acetone ($\geq$99.5%, Sigma Aldrich, Milan, Italy), were commercially available and used as supplied without any further purification. Milli-Q reagent water (18.2 MΩ cm, 25 °C, Millipore, Darmstadt, Germany) was used for all experiments.

3.2. Synthesis of $CoSb_2O_6$

Potassium antimony tartrate (1.6761 g) and $CoCl_2$ $6H_2O$ (0.3258 g) were weighed prior to grinding. To achieve a homogeneous mixture and reduce particle size, the powder was further treated with ball milling for 15 min. The resulting powder was then calcined in a porcelain crucible at temperatures ranging from 550 to 650 °C for 6 or 12 h under static air conditions, with a heating rate of 5 °C min^{-1}. Following calcination, the product was centrifuged in deionized water to separate and remove any byproducts. The final product was dried at room temperature.

3.3. Electrode Preparation for Activity and Stability Evaluation on GC-RDE

The working electrodes were prepared by employing the drop-casting technique to deposit the catalyst onto the surface of a glassy carbon rotating disk electrode (GC-RDE). Fresh ink was formulated to disperse the $CoSb_2O_6$ powder, typically comprising 2.0 mg of catalyst, 6 μL of Nafion (5 wt. % solution), and 300 μL of isopropyl alcohol (IPA). This mixture was sonicated for 30 min to ensure thorough dispersion.

3.4. Characterization Techniques

Powder X-ray diffraction (PXRD) measurements were conducted using an Empyrean Panalytical instrument (Baton Rouge, LA, USA) in a reflection–transmission spinner configuration to confirm the phase identity of the synthesized $CoSb_2O_6$ samples. The experimental parameters were as follows: Cu anode material, 2θ range of 10–80°, scan step size of 0.013° (2θ), tube current of 40 mA, generator voltage of 40 kV, and measurement temperature of 25 °C. The morphology of $CoSb_2O_6$ was analyzed using a ZEISS Supra 40 Field Emission Scanning Electron Microscope (FESEM). Elemental composition was quantified through Energy Dispersive X-ray Spectroscopy (EDS) using an in-house Oxford EDS microanalysis system with a Si (Li) detector cooled by liquid nitrogen. The specific surface area was determined by the Brunauer–Emmett–Teller (BET) method, and the total pore volume was calculated based on N_2 adsorption/desorption isotherms measured at 77 K using a Micromeritics (Norcross, GA, USA) TriStar 3020 volumetric analyzer.

3.5. Electrochemical Measurements

Electrocatalytic tests of the synthesized catalysts were performed in a rotating disk electrode (RDE) system to minimize mass transfer limitations and accurately assess the intrinsic kinetics of each catalyst. As illustrated in Figure 13, the experiments were carried out in a single-chamber cell in a three-electrode configuration. A glassy carbon electrode coated with the catalyst served as the working electrode (WE), an Ag/AgCl (3 M KCl) electrode as the reference electrode (RE), and a platinum wire as the counter electrode (CE). A Biologic VSP-300 multichannel potentiostat (POT) was used to control and measure the electrochemical parameters. The electrolyte consisted of 0.5 M H_2SO_4 (pH $\approx$ 0.3) to evaluate the performance and stability of the oxygen evolution reaction (OER) catalysts under highly acidic conditions.
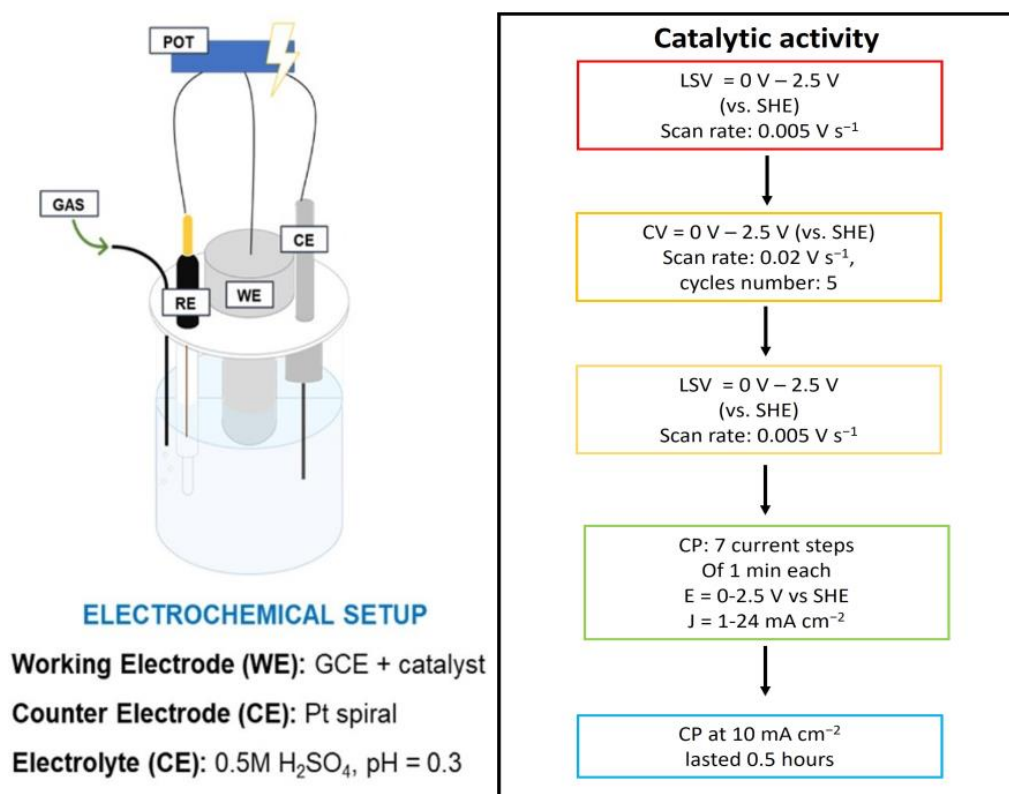
Figure 13. Setup and protocol used for the electrochemical analyses conducted on RDE system.

The protocol for testing OER catalytic activity and stability consisted of five steps divided into two separate deposition stages (see Figure 13). After each catalyst deposition, initial measurements of the Open Circuit Potential (OCP) and system resistance (ZIR) were taken. The first testing sequence began with an initial Linear Sweep Voltammetry (LSV$_0$), followed by five cyclic voltammetry (CV) cycles and a final LSV measurement (LSV$_1$) to assess any potential changes in catalytic activity compared to LSV$_0$. Subsequently, chronopotentiometry (CP) was conducted at seven different current densities to obtain potential data at each step, with ZIR measurements being performed at each potential to calculate overpotential and determine the Tafel slope, providing insights into catalytic activity and kinetics. Following this, a second catalyst deposition was applied, and the same sequence of tests was repeated from OCP to LSV$_1$. A final CP test, conducted for 30 min at a current density of 10 mA cm^{-2}, was carried out to evaluate the catalyst stability. The catalyst loading was varied (from 0.16 mg cm^{-2} to 0.50 mg cm^{-2} and 0.75 mg cm^{-2}), as was the rotating speed of the RDE system (from 1600 rpm to 2000 rpm), to optimize conditions for maximizing catalytic activity and minimizing mass transport limitations. Based on these results, subsequent tests were standardized to a catalyst loading of 0.75 mg cm^{-2} and a rotation speed of 1600 rpm. The electrochemical data presented in the work refer to the SHE potential, calculated with $E_{SHE} = E_{Ag/AgCl} + 0.209$ V.

4. Conclusions

In this work, we reported the critical aspects for the synthesis of CoSb$_2$O$_6$ as OER catalysts via solid-state reactions at six different combinations of calcination time and temperature. Regarding replicability, the detailed physico-chemical characterization carried out via BET, FESEM, PXRD, and EDX demonstrated the difficulty to obtain a 100% pure CoSb$_2$O$_6$ phase through the employed protocols. However, the developed catalysts demonstrated a high stability when employed as anodes for OER in acidic media, i.e.,

0.5 M H_2SO_4. According to their electrochemical analyses, the sample calcined at 600 °C for 6 h showed the best catalytic activity, i.e., the lowest overpotential, although it had the lowest specific surface area. Such performance was attributed to the maximized content of 110 facets (vs. 103) and the high content of $CoSb_2O_6$ (87 at.%).

This work provides a critical detailed investigation of different solid-state synthesis protocols to obtain $CoSb_2O_6$, the characterization of the obtained samples, and guidelines to improve the overall OER performance.

Supplementary Materials: The following supporting information can be downloaded at: https://www.mdpi.com/article/10.3390/catal15010068/s1, Figure S1: BET analyses, adsorption and desorption curves for $CoSb_2O_6$ synthetized at 550 °C, 600 °C, and 650 °C for 6 h; Table S1: Peaks intensity ratios, crystallite sizes, and estimation via Scherrer equation of crystallite sizes of $CoSb_2O_6$ samples calcined for 6 h; Figure S2: BET analyses, adsorption and desorption curves for $CoSb_2O_6$ synthetized at 550 °C, 600 °C, and 650 °C for 12 h; Table S2: Peaks intensity ratios, crystallite sizes, and estimation via Scherrer equation of the crystallite sizes of $CoSb_2O_6$ samples calcined for 12 h; Figure S3: BET analyses of $CoSb_2O_6$ samples calcined at 550 °C, 600 °C, and 650 °C for 6 and 12 h, reporting: (a) SSA; (b) average pore width; (c) average pore volume; Table S3: $CoSb_2O_6$ content in wt. % compared to the (Co+Sb)/O ratio; Figure S4: FESEM analyses and morphological study of $CoSb_2O_6$. All the samples shown were calcined for 6 h at: (a) 550 °C, (b) 600 °C, (c) 650 °C. The magnitude selected is of 50 kx; Figure S5: FESEM analyses and morphological study of $CoSb_2O_6$. All the samples shown were calcined for 12 h at: (a) 550 °C, (b) 600 °C, (c) 650 °C. The magnitude selected is of 50 kx. Table S4: PXRD analyses of $CoSb_2O_6$ samples. Phases composition in wt. % are reported; Table S5: EDX analyses, atomic % composition of $CoSb_2O_6$ samples synthetized at different temperatures and calcination times; Table S6: BET analyses of $CoSb_2O_6$ samples calcinated at 550 °C, 600 °C, and 650 °C for 6 and 12 h. The data shown below are related to the SSA, total pore volume, and average pore width; Table S7: RDE analyses, overpotentials at 10 mA cm^{-2} calculated with the data collected by the CPs under current steps; Table S8: Summary of state-of-the-art catalysts comparison with $CoSb_2O_6$. See references [30–35].

References

1. Song, F.; Bai, L.; Moysiadou, A.; Lee, S.; Hu, C.; Liardet, L.; Hu, C. Transition Metal Oxides as Electrocatalysts for the Oxygen Evolution Reaction in Alkaline Solutions: An Application-Inspired Renaissance. *J. Am. Chem. Soc.* **2018**, *140*, 7748–7759. [CrossRef]
2. Cook, T.R.; Dogutan, D.K.; Reece, S.Y.; Surendranath, Y.; Teets, T.S.; Nocera, D.G. Solar Energy Supply and Storage for the Legacy and Nonlegacy Worlds. *Chem. Rev.* **2010**, *110*, 6474–6502. [CrossRef] [PubMed]
3. Suen, N.T.; Hung, S.F.; Quan, Q.; Zhang, N.; Xu, Y.J.; Chen, H.M. Electrocatalysis for the oxygen evolution reaction: Recent development and future perspectives. *Chem. Soc. Rev.* **2017**, *46*, 337–365. [CrossRef] [PubMed]

4. Zhan, Y.; Lu, M.; Yang, S.; Xu, C.; Liu, Z.; Lee, J.Y. Activity of Transition-Metal (Manganese, Iron, Cobalt, and Nickel) Phosphates for Oxygen Electrocatalysis in Alkaline Solution. *ChemCatChem* **2016**, *8*, 372–379. [CrossRef]

5. An, L.; Wei, C.; Lu, M.; Liu, H.; Chen, Y.; Scherer, G.G.; Fisher, A.C.; Xi, P.; Xu, Z.J.; Yan, C. Recent Development of Oxygen Evolution Electrocatalysts in Acidic Environment. *Adv. Mater.* **2021**, *33*, 2006328. [CrossRef]

6. Lei, Z.; Wang, T.; Zhao, B.; Cai, W.; Liu, Y.; Jiao, S.; Li, Q.; Cao, R.; Liu, M. Recent Progress in Electrocatalysts for Acidic Water Oxidation. *Adv. Energy Mater.* **2020**, *10*, 2000478. [CrossRef]

7. Liu, W.; Kawano, K.; Kamiko, M.; Kato, Y.; Okazaki, Y.; Yamada, I.; Yagi, S. Effects of A-site Cations in Quadruple Perovskite Ruthenates on Oxygen Evolution Catalysis in Acidic Aqueous Solutions. *Small* **2022**, *18*, 2202439. [CrossRef] [PubMed]

8. Song, H.J.; Yoon, H.; Ju, B.; Kim, D.W. Highly Efficient Perovskite-Based Electrocatalysts for Water Oxidation in Acidic Environments: A Mini Review. *Adv. Energy Mater.* **2021**, *11*, 2002428. [CrossRef]

9. Ma, C.L.; Wang, Z.Q.; Sun, W.; Cao, L.M.; Gong, X.Q.; Yang, J. Surface Reconstruction for Forming the [IrO$_6$]–[IrO$_6$] Framework: Key Structure for Stable and Activated OER Performance in Acidic Media. *ACS Appl. Mater. Interfaces* **2021**, *13*, 29654–29663. [CrossRef] [PubMed]

10. Liu, Y.; Chen, Y.; Mu, X.; Wu, Z.; Jin, X.; Li, J.; Xu, Y.; Yang, L.; Xi, X.; Jang, H.; et al. Spinel-Anchored Iridium Single Atoms Enable Efficient Acidic Water Oxidation via Intermediate Stabilization Effect. *ACS Catal.* **2023**, *13*, 3757–3767. [CrossRef]

11. Zhao, Y.; Wan, W.; Erni, R.; Pan, L.; Patzke, G.R. Operando Spectroscopic Monitoring of Metal Chalcogenides for Overall Water Splitting: New Views of Active Species and Sites. *Angew. Chem. Int. Ed. Engl.* **2024**, *63*, e202400048. [CrossRef] [PubMed]

12. Chen, D.; Liu, T.; Wang, P.; Zhao, J.; Zhang, C.; Cheng, R.; Li, W.; Ji, P.; Pu, Z.; Mu, S. Ionothermal Route to Phase-Pure RuB$_2$ Catalysts for Efficient Oxygen Evolution and Water Splitting in Acidic Media. *ACS Energy Lett.* **2020**, *5*, 2909–2915. [CrossRef]

13. Gao, X.; Zhou, H.; Wang, Z.; Zhou, G.; Wang, J.; Wu, Y. Acid-Stable Antimonate based Catalysts for the Electrocatalytic Oxygen Evolution Reaction. *Nano Res.* **2023**, *16*, 4691–4697. [CrossRef]

14. Parsons, R. Atlas of electrochemical equilibria in aqueous solutions. *J. Electroanal. Chem. Interfacial Electrochem.* **1967**, *13*, 471. [CrossRef]

15. Weber, M.F.; Dignam, M.J. Efficiency of Splitting Water with Semiconducting Photoelectrodes. *J. Electrochem. Soc.* **1984**, *131*, 1258. [CrossRef]

16. Mondschein, J.S.; Callejas, J.F.; Read, C.G.; Chen, J.Y.C.; Holder, C.F.; Badding, C.K.; Schaak, R.E. Crystalline Cobalt Oxide Films for Sustained Electrocatalytic Oxygen Evolution under Strongly Acidic Conditions. *Chem. Mater.* **2017**, *29*, 950–957. [CrossRef]

17. Tamaki, J.; Yamada, Y.; Yamamoto, Y.; Matsuoka, M.; Ota, I. Sensing properties to dilute hydrogen sulfide of ZnSb2O6 thick-film prepared by dip-coating method. *Sens. Actuators B Chem.* **2000**, *66*, 70–73. [CrossRef]

18. Wu, S.; Li, G.; Zhang, Y.; Zhang, W. Surface photoelectric and visible light driven photocatalytic properties of zinc antimonate-based photocatalysts. *Mater. Res. Bull.* **2013**, *48*, 1117–1121. [CrossRef]

19. Jang, J.; Kim, S.J. Photoelectrochemical Properties of Nanocrystalline Sb$_6$O$_{13}$, MgSb$_2$O$_6$, and ZnSb$_2$O$_6$-Based Electrodes for Dye-Sensitized Solar Cells. *Jpn. J. Appl. Phys.* **2012**, *51*, 10NE23. [CrossRef]

20. Evans, T.A.; Choi, K.S. Electrochemical Synthesis and Investigation of Stoichiometric, Phase-Pure CoSb$_2$O$_6$ and MnSb$_2$O$_6$ Electrodes for the Oxygen Evolution Reaction in Acidic Media. *ACS Appl. Energy Mater.* **2020**, *3*, 5563–5571. [CrossRef]

21. Sunku, M.; Gundeboina, R.; Shilpa Chakra, C.H.; Kaniki Reddy, V.; Vithal, M. Preparation, characterization and photocatalytic activity studies of C- and N- doped CoSb$_2$O$_6$. *Inorg. Chem. Commun.* **2021**, *134*, 109064. [CrossRef]

22. Li, D.-H.; He, S.-F.; Chen, J.; Jiang, C.-Y.; Yang, C. Solid-state Chemical Reaction Synthesis and Characterization of Lanthanum Tartrate Nanocrystallites Under Ultrasonication Spectra. *IOP Conf. Ser. Mater. Sci. Eng.* **2017**, *242*, 012023. [CrossRef]

23. Babaei, A.; Rezaei, M. Development of a highly stable and active non-precious anode electrocatalyst for oxygen evolution reaction in acidic medium based on nickel and cobalt-containing antimony oxide. *J. Electroanal. Chem.* **2023**, *935*, 117319. [CrossRef]

24. Michel, C.R.; Martínez-Preciado, A.H.; Morán-Lázaro, J.P. Effect of the frequency on the gas sensing response of CoSb$_2$O$_6$ prepared by a colloidal method. *Sens. Actuators B Chem.* **2009**, *140*, 149–154. [CrossRef]

25. Jovic, M.; Dasic, M.; Holl, K.; Ilic, D.; Mentus, S. Gel-combustion synthesis of CoSb$_2$O$_6$ and its reduction to powdery Sb$_2$Co alloy. *J. Serb. Chem. Soc.* **2009**, *74*, 53–60. [CrossRef]

26. Michel, C.R.; Guillén-Bonilla, H.; Martínez-Preciado, A.H.; Morán-Lázaro, J.P. Synthesis and gas sensing properties of nanostructured CoSb$_2$O$_6$ microspheres. *Sens. Actuators B Chem.* **2009**, *143*, 278–285. [CrossRef]

27. Guillén-Bonilla, A.; Rodríguez-Betancourtt, V.-M.; Flores-Martínez, M.; Blanco-Alonso, O.; Reyes-Gómez, J.; Gildo-Ortiz, L.; Guillén-Bonilla, H. Dynamic Response of CoSb$_2$O$_6$ Trirutile-Type Oxides in a CO$_2$ Atmosphere at Low-Temperatures. *Sensors* **2014**, *14*, 15802–15814. [CrossRef]

28. Degen, T.; Sadki, M.; Bron, E.; König, U.; Nénert, G. The HighScore suite. *Powder Diffr.* **2014**, *29*, S13–S18. [CrossRef]

29. Gunasooriya, G.T.K.K.; Kreider, M.E.; Liu, Y.; Zeledón, J.A.Z.; Wang, Z.; Valle, E.; Yang, A.-C.; Gallo, A.; Sinclair, R.; Stevens, M.B.; et al. First-Row Transition Metal Antimonates for the Oxygen Reduction Reaction. *ACS Nano* **2022**, *16*, 6334–6348. [CrossRef]

30. Mondschein, J.S.; Kumar, K.; Holder, C.F.; Seth, K.; Kim, H.; Schaak, R.E. Intermetallic Ni2Ta Electrocatalyst for the Oxygen Evolution Reaction in Highly Acidic Electrolytes. *Inorg. Chem.* **2018**, *57*, 6010–6015. [CrossRef] [PubMed]

31. Safdar, M.; Iftikhar, M.; Rashid, S.; Awais, M.; Iqbal, A.; Bilal, A.; Aslam, S.; Mirza, M. Synthesis and investigation of catalytic HER/OER performances of Al2SSe in alkaline/acidic media and water detoxification behavior. *Int. J. Hydrogen Energy* **2023**, *50*, 107–117. [CrossRef]

32. Lei, C.; Chen, H.; Cao, J.; Yang, J.; Qiu, M.; Xia, Y.; Yuan, C.; Yang, B.; Li, Z.; Zhang, X.; et al. Fe-N$_4$ Sites Embedded into Carbon Nanofiber Integrated with Electrochemically Exfoliated Graphene for Oxygen Evolution in Acidic Medium. *Adv. Energy Mater.* **2018**, *8*, 1801912. [CrossRef]

33. Doan, T.L.L.; Nguyen, D.C.; Prabhakaran, S.; Kim, D.H.; Tran, D.T.; Kim, N.H.; Lee, J.H. Single-Atom Co-Decorated MoS$_2$ Nanosheets Assembled on Metal Nitride Nanorod Arrays as an Efficient Bifunctional Electrocatalyst for pH-Universal Water Splitting. *Adv. Funct. Mater.* **2021**, *31*, 2100233. [CrossRef]

34. Chang, S.Q.; Cheng, C.C.; Cheng, P.Y.; Huang, C.L.; Lu, S.Y. Pulse electrodeposited FeCoNiMnW high entropy alloys as efficient and stable bifunctional electrocatalysts for acidic water splitting. *Chem. Eng. J.* **2022**, *446*, 137452. [CrossRef]

35. Wang, Y.; Jiao, Y.; Yan, H.; Yang, G.; Tian, C.; Wu, A.; Liu, Y.; Fu, H. Vanadium-Incorporated CoP$_2$ with Lattice Expansion for Highly Efficient Acidic Overall Water Splitting. *Angew. Chem.* **2022**, *134*, e202116233. [CrossRef]